Signatures of magnetostriction and spin-phonon coupling in magnetoelectric hexagonal 15*R*-BaMnO₃

Bommareddy Poojitha ⬤, Anjali Rathore ⬤, Ankit Kumar ⬤, and Surajit Saha ⬤[*]

Department of Physics, Indian Institute of Science Education and Research, Bhopal 462066, India

Spin-phonon coupling, the interaction of spins with a surrounding lattice, is a key parameter to understand the underlying physics of multiferroics and to engineer their magnetization dynamics. Elementary excitations in multiferroic materials are strongly influenced by spin-phonon interaction, making Raman spectroscopy a unique tool to probe these coupling(s). Recently, it has been suggested that the dielectric and magnetic properties of 15*R*-type hexagonal BaMnO₃ are correlated through the spin-lattice coupling. Here, we report the observation of an extensive renormalization of the Raman spectrum of 15*R*-BaMnO₃ at 230, 280, and 330 K. Magnetic measurements reveal the presence of a long-range and a short-range magnetic ordering in 15*R*-BaMnO₃ at 230 and 330 K, respectively. The Raman spectrum shows the appearance of new Raman modes in the magnetically ordered phases. Furthermore, an additional Raman phonon appears below ∼ 280 K, possibly arising from a local lattice distortion due to the displacement of Mn ions, that exhibits an anomalous shift with temperature. The origin of the observed renormalization and phonon anomalies in Raman spectra are discussed based on the evidence from temperature- and magnetic-field-dependent Raman spectra, temperature-dependent x-ray diffraction, magnetization, and specific-heat measurements. Our results indicate the presence of magnetostriction and spin-phonon coupling in 15*R*-BaMnO₃, thus suggesting that the optical phonons are strongly correlated to its magnetoelectric properties.

I. INTRODUCTION

The coupling among various degrees of freedom, such as spin, charge, lattice, and orbital, is important as it gives rise to various novel phenomena and it leads to exotic ground states in condensed-matter systems [1–4]. The interplay between phonons and electron spins is relevant for many exotic phenomena including the spin-Peierls transition, the phonon Hall effect, colossal magnetoresistance, ultrafast magnetization control, the spin Seebeck effect, etc. [1–5] Recently, there has been a renewed interest in studying spin-phonon coupling (SPC) within the context of multiferroics and spintronics. In multiferroic materials, SPC has been implored to explain compelling phenomena such as the thermal Hall effect [6]. Moreover, SPC allows tailoring the functionalities of transition-metal oxides such as stabilizing a new multiferroic ground state by applying strain, tuning to unusual magnetic ground states, etc. SPC also provides useful information about spin relaxation time, which is an important concern in spintronics applications such as quantum computing [7–13]. Unfortunately, the number of candidate (multiferroic) materials is limited, and it often happens that either the transitions are at very low temperatures or the response of cross-coupling between ferroic orders is too weak to be useful in device applications [14]. Hence, the search for new multiferroic materials with better functionalities has been ongoing.

In this context, 15*R*-type hexagonal BaMnO₃ (15*R*-BaMnO₃) has received a renewed importance since the discovery of a magnetoelectric property near room temperature [15], exhibiting antiferromagnetism below (T_N) ∼ 230 K. It is considered to be an exceptional class of magnetoelectrics due to the fact that both the electric and magnetic properties are associated with the same Mn⁺⁴ ions. The electric polarization arises from the displacement of the same ions (magnetic ions, Mn⁴⁺) along the *c*-axis, akin to that of classic ferroelectric material BaTiO₃. It was believed that the asymmetric environment of Mn ions within MnO₆ octahedra in the cubic and hexagonal layers leads to ferroelectric instability in the lattice, which also has an intimate connection with magnetic ordering [15]. Korneta *et al.* observed that both magnetization and the dielectric constant are highly anisotropic, and the in-plane (*ab*-plane) dielectric constant is sensitive to an applied magnetic field [15]. They attributed the observed correlation between magnetic and dielectric responses to the possible spin-phonon coupling in 15*R*-BaMnO₃. Since phonons play a major role in ferroelectric materials [16–18], one may expect them to have an equally important role in magnetoelectric multiferroics, too. A detailed understanding of the phonons and their coupling is, therefore, extremely important as it extends the opportunity to engineer new functionalities in transition-metal oxides such as BaMnO₃ and others.

The idiosyncratic feature of spin-phonon coupling is the renormalization of phonon parameters. The electron spin can interact with its surrounding lattice in a number of possible ways, e.g., the lattice vibrations involving Mn-O or Mn-O-Mn bonds modify spin-spin correlations through superexchange

interactions in antiferromagnets [19–21]. Similarly, if spins are coupled to elastic degrees of freedom, spontaneous strain occurs at magnetic transition temperature, giving rise to magnetostriction [22]. Multiferroic properties are associated with the lowering of symmetries (spatial and time-reversal symmetry). Since Raman spectroscopy is sensitive to these changes, it emerges as a powerful tool to detect the presence of coupling between different degrees of freedom, e.g., magnetostriction, spin-phonon coupling, electron-phonon coupling, etc., in strongly correlated multifunctional materials [11,12,22,23]. In this article, we have investigated the correlation between the phonons and magnetoelectric properties of $15R$-BaMnO$_3$. Temperature-dependent magnetization measurements reveal two magnetic transitions: a possible short-range ordering at $T_S \sim 330(\pm 0.2)$ K, hitherto unknown, and a long-range antiferromagnetic ordering at $T_N \sim 230(\pm 0.2)$ K. We have observed six Raman-active modes responding to the magnetic transitions at T_S (short-range ordering) and T_N (antiferromagnetic ordering), which can be attributed to spin-phonon coupling and magnetostriction. Additionally, a new phonon mode emerges in the Raman spectra at temperatures below $T_D \sim 280$ K, indicating a local lattice distortion possibly arising from displacements of the Mn ions, the frequency that exhibits anomalous softening with decreasing temperature. The magnetic-field dependence of the Raman modes and temperature-dependent x-ray diffraction measurements corroborate our observations. The strength of spin-phonon coupling is estimated by a model based on mean-field and two-spin cluster approximations. The origin of strong renormalization of the Raman-active phonons below the magnetic transitions (T_S/T_N) is discussed in detail.

II. EXPERIMENTAL DETAILS

Polycrystalline samples of $15R$-BaMnO$_3$ were synthesized by using the solid-state reaction method. High-purity BaCO$_3$ (99.999%) and MnO$_2$ (99.99%) (Sigma-Aldrich) powders were used as precursors. The stoichiometric mixture was ground well for 3 h and calcined at 1250 and 1300 °C for 2 h each with intermediate grindings. After the calcination, the resultant powder was ground, pelletized, and sintered at 1400 °C for 6 h. Powder x-ray diffraction (PXRD) measurements were done with a PANalytical Empyrean x-ray diffractometer with Cu $K\alpha$ radiation of wavelength 1.5406 Å. A liquid-nitrogen-based Anton Paar TTK 450 heating stage was used to control the sample-temperature during nonambient PXRD measurements. Chemical compositions were determined using the energy-dispersive x-ray analysis (EDAX) technique equipped with a high-resolution field emission scanning electron microscope (HR-FESEM) (Zeiss ULTRA Plus). Transmission electron microscopy (TEM) images were collected to verify the periodicity in the lattice using TALOS S-FEG [Schottky FEG (field emission gun–transmission electron microscope)] emitter with an accelerating voltage of 200 kV. For the TEM measurement of the samples, a small amount of the powder sample of the as-synthesized compound was dispersed in distilled water by ultrasonicating for 20 s. This (turbid) solution was then drop-casted on a carbon-coated copper grid forming a very thin layer. The solution/layer was then allowed

to dry for a few hours thoroughly before it was attached to the sample holder on the microscope (TEM) for viewing. Raman spectra were collected from pelletized samples in the backscattering configuration using a LabRAM HR Evolution Raman spectrometer attached with a frequency-doubled Nd:YAG (neodymium-doped yttrium aluminum garnet; Nd : Y$_3$Al$_{l5}$O$_{12}$) laser excitation source of wavelength 532 nm and a Peltier cooled charge-coupled device (CCD) detector. A microscope objective of 50× magnification and a numerical aperture of 0.5 was used to collect the scattered light. A Linkam stage (Model HFS600E-PB4) was used for variable temperature Raman measurements. The Raman spectrometer was also optically coupled to a closed-cycle cryomagnet (Attocube 1000) to measure magnetic-field-dependent Raman spectra at low temperature. dc magnetization measurements as a function of temperature and external magnetic field were carried out using a Quantum Design SQUID-VSM (superconducting quantum interference device with vibrating sample magnetometer). Specific heat (C_p) measurements were performed using a commercial Quantum Design PPMS on thin, flat pellet samples in the temperature range 5–390 K. Data were collected in two different runs: the data from 5 to 295 K were collected in the first run where Apiezon N-grease was used (to stick the sample to the holder) as an addenda, and the high-temperature data (295–390 K) were collected in the second run, which required an additional oven attachment and Apiezon H-grease (glue to stick the sample to the holder) as an addenda. The data were collected during the heating cycle. Measurement on the sample was preceded by a measurement of the addenda in the same temperature range following a thermal relaxation method. The heat capacity (C_p) of the sample was obtained after subtracting the addenda heat capacity from the total heat capacity.

III. RESULTS AND DISCUSSION

A. Structural and magnetic properties

The crystal structure of $15R$-BaMnO$_3$, drawn using VESTA (Visualization of Electronic and STructural Analysis) software [24], is shown in Fig. 1(a). It contains 15 formula units (75 atoms) per unit cell and 5 formula units (25 atoms) per primitive cell. The $15R$ unit cell possesses an intermediate structure between an ideal cubic (c) and hexagonal (h) structure with a layer stacking sequence of $(chhhh)_3$, or in other words, atomic stacking of "ABCBACABACBAACB." The corner-shared connectivity (cubic to hexagonal stacking ratio) is 20%. It has Mn$_5$O$_{18}$ units (of five face-shared octahedra) connected to each other directly at their corners, forming a chain along the c-axis [Fig. 1(a)]. The crystal phase and corresponding unit-cell parameters for the synthesized sample are obtained from Rietveld refinement of the room-temperature x-ray diffraction patterns using High-score Plus software. The refinement indicates that the synthesized compound is in $15R$-type hexagonal phase possessing R-3m (no. 166) space group with rhombohedral symmetry. No additional or unexpected reflections could be identified, thus confirming that the synthesized powder is of single-phase and free from any detectable impurity. The refined lattice parameters at room temperature are $a = b = 5.6817$ Å, $c = 35.369$ Å,
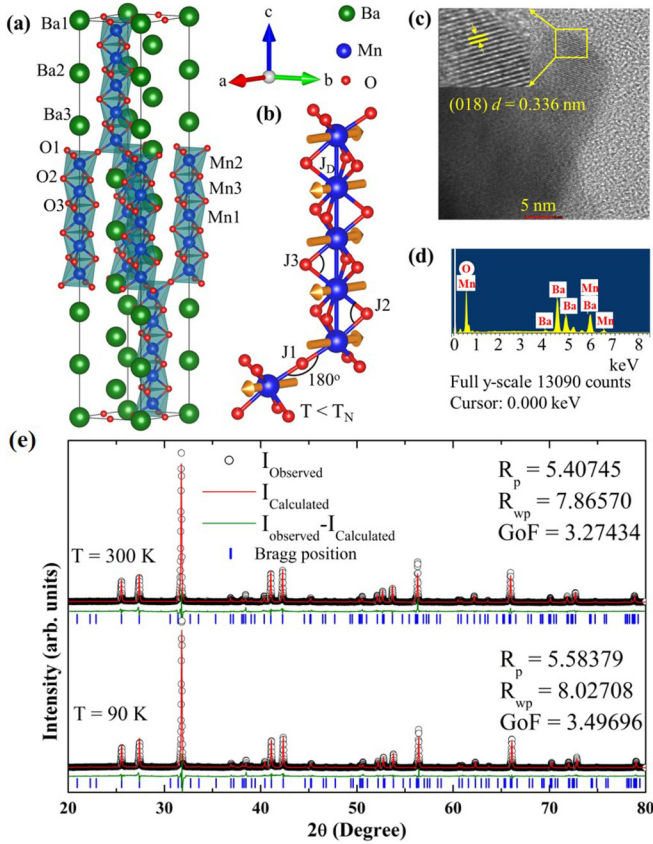
FIG. 1. (a) Crystallographic unit cell of 15R-BaMnO$_3$, (b) spin arrangement of Mn ions in antiferromagnetic phase, (c) TEM image showing the lattice planes, (d) EDAX spectrum showing the stoichiometric presence of the elements, and (e) x-ray diffraction patterns collected at 300 and 90 K. R-factors (R_p and R_{wp}) and the goodness of fit (GoF) obtained from the refinements are also given.

TABLE I. Lattice parameters, bond lengths, and bond angles of 15R-BaMnO$_3$ obtained from the Rietveld refinement of x-ray diffraction data at room temperature.

Lattice parameters	$a = b = 5.6817$ Å, $c = 35.369$ Å, $\alpha = \beta = 90°$, $\gamma = 120°$	
Bond lengths	Mn2-Mn2	3.8406 Å
	Mn2-Mn3	2.4783 Å
	Mn3-Mn1	2.4178 Å
	Mn2-O1	1.9203 Å
	Mn2-O2	1.9294 Å
	Mn3-O2	1.8834 Å
	Mn3-O3	1.9248 Å
	Mn1-O3	1.9055 Å
Bond angles	Mn1-O1-Mn1	180°
	Mn2-O2-Mn3	81.07°
	Mn3-O3-Mn1	78.28°

$\alpha = \beta = 90°$, and $\gamma = 120°$, which are comparable to the previous reports [15,25,26]. Three irreducible sites each for Ba, Mn, and O atoms in the unit cell, which are labeled as Ba1,Ba2,Ba3, Mn1,Mn2,Mn3, and O1,O2,O3, respectively, are shown in Fig. 1(a). The bond lengths and angles are listed in Table I. The refined crystallographic Wyckoff positions for each atom are listed in Table S1 in the Supplemental Material [27]. The Mn-Mn distance along the face-shared octahedra (2.4178–2.4783 Å) is comparable to or smaller than the metallic γ-Mn (2.47 Å), which plays an important role in the physical properties of BaMnO$_3$ [28]. The strong electrostatic repulsion between Mn atoms leads to distortion in face-shared octahedra making them asymmetric while corner-shared octahedra remain symmetric with all six Mn-O bonds of equal lengths (Table I) [15]. The spin arrangement in the magnetically ordered phase is displayed in Fig. 1(b), which implies that the spins orient along the a-axis and are antiferromagnetically ordered along the c-axis [15], which will be discussed later. TEM images also confirm the formation of the lattice structure of the compound [Fig. 1(c)]. The d-spacing and lattice parameters are estimated and found to be in agreement with our PXRD results. EDAX measurements were carried out for elemental analysis, the details of which

are given in Fig. 1(d) and Table II. We found no detectable impurity elements or additional phases in the sample (see the Supplemental Material for further details [27]).

To investigate the spin-ordering transitions, temperature-dependent magnetization measurements were carried out in two different protocols: zero-field cooling (ZFC) and field cooling (FC) under the applied field of 500 Oe as shown in Fig. 2(a). The transition temperatures can be clearly determined from the inflection in the derivative, $\frac{dM(T)}{dT}$, shown in the inset of Fig. 2(a). Our data show two magnetic transitions: one as an anomaly at 330 (± 0.2) K and another at 230 (± 0.2) K, which are, respectively, the outcomes of a short-ranged direct exchange interaction (J_D) between Mn^{+4} ions in face-shared MnO$_6$ octahedra of the Mn$_5$O$_{18}$ units and linear Mn-O-Mn superexchange ($J1$) between Mn^{+4} ions located in corner-shared octahedra [29]. The bond angles for Mn2-O2-Mn3 and Mn3-O3-Mn1 are 81.07° and 78.28°, respectively, where the overlapping between 3d orbitals of Mn^{+4} and O-2p orbitals is minimal, resulting in relatively weak and negligible ferromagnetic (FM) exchange interactions that are denoted by $J2$ and $J3$, respectively [Fig. 1(b)]. Notably, the heat capacity as a function of temperature [Fig. 2(b)] shows two anomalies (*kinks*) at $\sim$ 330 (± 0.2) and $\sim$ 230 (± 0.2) K corresponding to the two magnetic transitions, thus corroborating our magnetization results. The observed low-temperature magnetic transition at $\sim$ 43 (± 0.2) K is associated with spin canting (see Figs. S1–S4 in Sec. SM2 of the Supplemental Material [27] for further details, including field-dependent magnetization results and further analysis on magnetic transitions) [30,31]. Below 230 K (T_N), the spins orient along the a-axis and are antiferromagnetically ordered along the c-axis exhibiting an in-plane parallel arrangement with no direct exchange pathways, as shown in Fig. 1(b) (spin alignment in the full unit cell is shown in Fig. S2 of the Supplemental Material [27]). To understand the correlation between the phonons and magnetoelectric order parameters, we have performed a

TABLE II. EDAX data of 15R-BaMnO$_3$.

	EDAX results	
Element	Weight%	Atomic%
O K	22.00 ($\pm$0.08)	63.47 ($\pm$0.09)
Mn K	20.43 ($\pm$0.13)	17.17 ($\pm$0.13)
Ba L	57.57 ($\pm$0.14)	19.36 ($\pm$0.06)
Total	100.00	100

systematic Raman spectroscopic measurement with varying temperature and magnetic field as discussed below.

B. Raman spectroscopy

According to group theory, the 15R structure with the space group R-$3m$ leads to 18 Raman-active and 27 IR-active phonons at the Γ point of the Brillouin zone with irreducible representations $\Gamma_{\text{Raman}} = 8A_{1g} + 10E_g$ and $\Gamma_{\text{IR}} = 12A_{2u} + 15E_u$, respectively (Tables III and S2). Because of the site symmetries, the atoms Ba1, Mn1, and O1 participate only in IR-active vibrations and are not involved in Raman-active
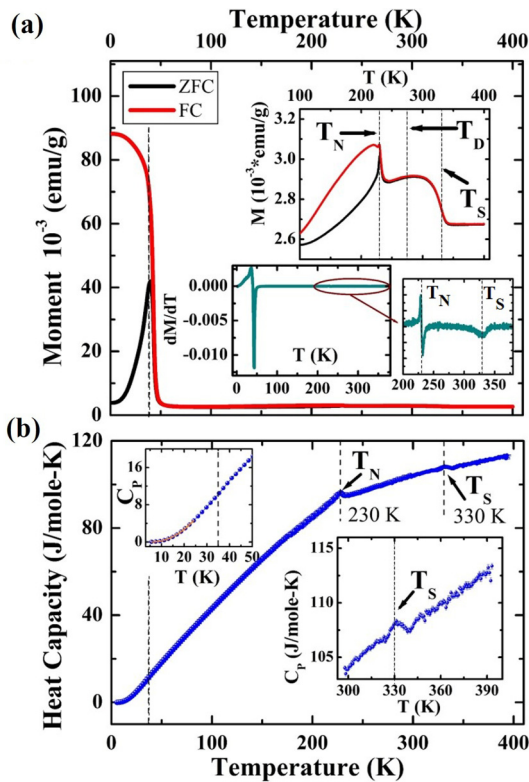

FIG. 2. (a) Magnetic moment as a function of temperature, and insets show enlarged view in high-temperature range and the temperature derivative of magnetization to clearly identify the antiferromagnetic transition temperatures. (b) Temperature-dependent heat capacity; the left inset is an enlarged view of the heat capacity (C_P) in the low-temperature range (the orange solid line is a fit with $C_P(T) = \beta T^3 + \delta T^2$ [Eq. (S2)] explained in the Supplemental Material [27] suggesting A-type or canted antiferromagnetic ordering at these temperatures), and the right inset clearly shows the response at $T_S \sim 330$ K.

modes, whereas Ba2, Ba3, Mn2, Mn3, O2, and O3 take part in both IR- and Raman-active vibrations. Figure 3(a) shows the Raman spectra collected at room temperature (300 K) and 80 K along with their Lorentzian fits. The symmetry assignment of the modes is done based on our polarization-dependent Raman spectra (Fig. S5 in the Supplemental Material [27]), SYMMODES-Bilbao Crystallographic Server [32], and previous reports [26,33]. The spectrum at 80 K presents an additional number of modes as compared to the one collected at 300 K, implying the possible association with a change in the crystallographic and/or magnetic symmetry of BaMnO$_3$ at low temperatures [34–37]. To get a better understanding of the phonons, we have collected Raman spectra systematically in the temperature range of 80–800 K and analyzed their evolution by fitting with Lorentzian multifunction. The Raman spectra at a few typical temperatures are shown in Fig. S6 of the Supplemental Material [27]. The phonon parameters (spectral weight/intensity, frequency, and linewidth) as a function of temperature for a few selected modes are displayed in Fig. 3. The spectral weight (intensity) decreases with increasing temperature for almost all the modes, possibly because the temperature dependence of intensity due to the Bose factor is masked by the temperature dependence of the absorption coefficient (the intensity of the other modes is shown in Fig. S7 in the Supplemental Material [27]) [38]. The frequency and linewidth of the majority of phonons show the usual anharmonic trend [i.e., a decrease (increase) in mode frequency (linewidth) with increasing temperature] as shown in Figs. S8 and S9 in the Supplemental Material [27]. Notably, these modes exhibit a change in slope at one of the magnetic transition temperatures (T_N or T_S) or at a temperature $T_D \sim 280$ K. More importantly, five of the phonon modes (namely P7, P8, P12, P14, and P15) are observed to respond drastically at these temperatures, as shown in Fig. 3. The mode P7 at ~ 390 cm^{-1} vanishes right above $T_D \sim 280$ K. We attribute the origin of P7 mode to the displacement of Mn^{+4} ions along the c-axis amounting to a change in local symmetry that may be associated with the dielectric anomaly reported in Ref. [15]. The frequency (of mode P7) shows an anomalous temperature dependence (i.e., a decrease in frequency with decreasing temperature) while the linewidth shows an extremely large broadening (by almost fourfold) in the temperature range of 80–280 K. The anomalies in P7 could be related to spin-phonon coupling to be discussed later. On the other hand, the P12 and P14 modes appear right below the magnetic transitions T_N and T_S, respectively. In addition, each of the modes at ~ 415 cm^{-1} (P8) and ~ 653 cm^{-1} (P15) clearly splits into two modes right below $T_N \sim 230(\pm 0.2)$ K. Note that our temperature-dependent x-ray diffraction measurements (to be discussed later) show no clear signatures of structural phase transition in the investigated temperature range (90–400 K), thus ruling out structural phase transition as the possible origin for the splitting of the two modes P8 and P15. However, the possibilities of further changes in the local symmetries at T_N arising from additional displacements of Mn ions cannot be completely ruled out. Further, the mode P6 deviates from the anharmonic trend (discussed below) at temperatures below T_N (similar to the deviations seen for the other modes below $T_N/T_S/T_D$, shown in Figs. S8 and S9 [27]). These observations suggest the presence of a strong correlation between

TABLE III. Raman-active phonons in 15R-BaMnO$_3$.

Space group R-$3m$ (No. 166) and $\Gamma_{\text{Raman}} = 8A_{1g} + 10E_g$		Wyckoff positions 6c (Ba2, Ba3) 6c (Mn2, Mn3) 18h (O2, O3)		Irreducible representations $2A_{1g} + 2E_g$ $2A_{1g} + 2E_g$ $4A_{1g} + 6E_g$
Mode	Symmetry	ω(cm^{-1})		Atoms involved in the vibration
		at 80 K	at 300 K	
P1	E_g	82.0 ($\pm$0.1)	80.9 ($\pm$0.1)	Ba
P2	A_{1g}	100.7 ($\pm$0.1)	99.3 ($\pm$0.1)	Ba
P3	E_g	176.5 ($\pm$0.1)	174.7 ($\pm$0.1)	Ba
P4	E_g	241.8 ($\pm$0.1)	238.9 (0.1)	Mn
P5	E_g	278.5 ($\pm$0.1)	275.6 ($\pm$0.1)	Mn
P6	E_g	361.4 ($\pm$0.1)	358.4 ($\pm$0.1)	Mn
P7	A_{1g}	383.5 ($\pm$0.2) (Appears at $T < 280$ K)	Absent	Mn
P8A	A_{1g}	418.2 ($\pm$0.1)	P8: 415.3	O
P8B	A_{1g}	422.0 ($\pm$0.1) (Appears at $T < 230$ K)	($\pm$0.1) (E_g)	
P9	E_g	430.3 ($\pm$0.1)	427.5 ($\pm$0.1)	O
P10	A_{1g}	535.6 ($\pm$0.4)	530.0 ($\pm$0.4)	O
P11	E_g	557.9 ($\pm$0.1)	552.2 ($\pm$0.1)	O
P12	E_g	565.9 ($\pm$0.1) (Appears at $T < 230$ K)	Absent	O
P13	E_g	583.0 ($\pm$0.1)	578.8 ($\pm$0.1)	O
P14	A_{1g}	643.2 ($\pm$0.1)	636.9 ($\pm$0.3)	O
P15A	A_{1g}	655.8 ($\pm$0.1)	P15: 653.3	O
P15B	A_{1g}	659.9 ($\pm$0.4) (Appears at $T < 230$ K)	($\pm$0.1) (E_g)	

phonons and magnetoelectric parameters in 15R-BaMnO$_3$. To understand the origin of phonon anomalies and the appearance of new peaks in Raman spectra below magnetic transitions, we have analyzed the temperature dependence of phonon frequency and linewidth using the anharmonic model.

In general, the temperature dependence of a phonon frequency can be written as [39–42]

$$\omega(T) = \omega_{\text{anh}}(T) + \Delta\omega_{\text{el-ph}}(T) + \Delta\omega_{\text{sp-ph}}(T). \quad (1)$$

The first term $\omega_{\text{anh}}(T)$ is the anharmonic contribution as discussed below. The contribution to the change in phonon frequency due to electron-phonon coupling is given by the term $\Delta\omega_{\text{el-ph}}(T)$, which is absent in 15$R$-BaMnO$_3$ due to its insulating nature. The renormalization of the frequency due to spin-phonon coupling is denoted by $\Delta\omega_{\text{sp-ph}}(T)$. In the cubic anharmonic process, the phonon of frequency ω_0 decays into two phonons of equal frequency $\omega_0/2$ satisfying the energy and momentum conservation. The temperature dependence of the phonon frequency due to cubic anharmonicity (three-phonon process) is given by [39,40]

$$\omega_{\text{anh}}(T) = \omega_0 + A\left[1 + \frac{2}{\left(e^{\frac{\hbar\omega_0}{2k_BT}} - 1\right)}\right]. \quad (2)$$

Similarly, the temperature dependence of phonon linewidth due to cubic anharmonicity can be written as

$$\Gamma_{\text{anh}}(T) = \Gamma_0 + C\left[1 + \frac{2}{\left(e^{\frac{\hbar\omega_0}{2k_BT}} - 1\right)}\right], \quad (3)$$

where ω_0 and Γ_0 are the frequency and linewidth of the phonon at absolute zero temperature, respectively, A and C are cubic anharmonic coefficients for frequency and linewidth, respectively, $\hbar$ is the reduced Planck constant, k_B is the Boltzmann constant, and T is the variable temperature. As seen in our data, both the frequency and the linewidth of almost all the phonons show a finite deviation from the anharmonic temperature dependence, indicating the possible magnetostriction in the system [Figs. 3(c) and 3(d), and Figs. S8 and S9 [27]]. The solid lines in Figs. 3(c) and 3(d) represent the fitting with Eqs. (2) and (3). The mode P12 appears below T_N (origin to be discussed later), and its frequency and linewidth exhibit the expected thermal behavior [Eqs. (2) and (3), respectively]. Most importantly, the mode P7 that appears below T_D shows an anomalous shift in frequency while its linewidth undergoes an anomalous broadening that cannot be explained by anharmonicity alone. These indicate the strong role of spin-phonon coupling. Further, the P6 and P14 modes show a deviation from anharmonic thermal behavior in their temperature dependence of frequency and linewidth at low temperatures below the Néel temperature $T_N \sim 230$ K. In the absence of any
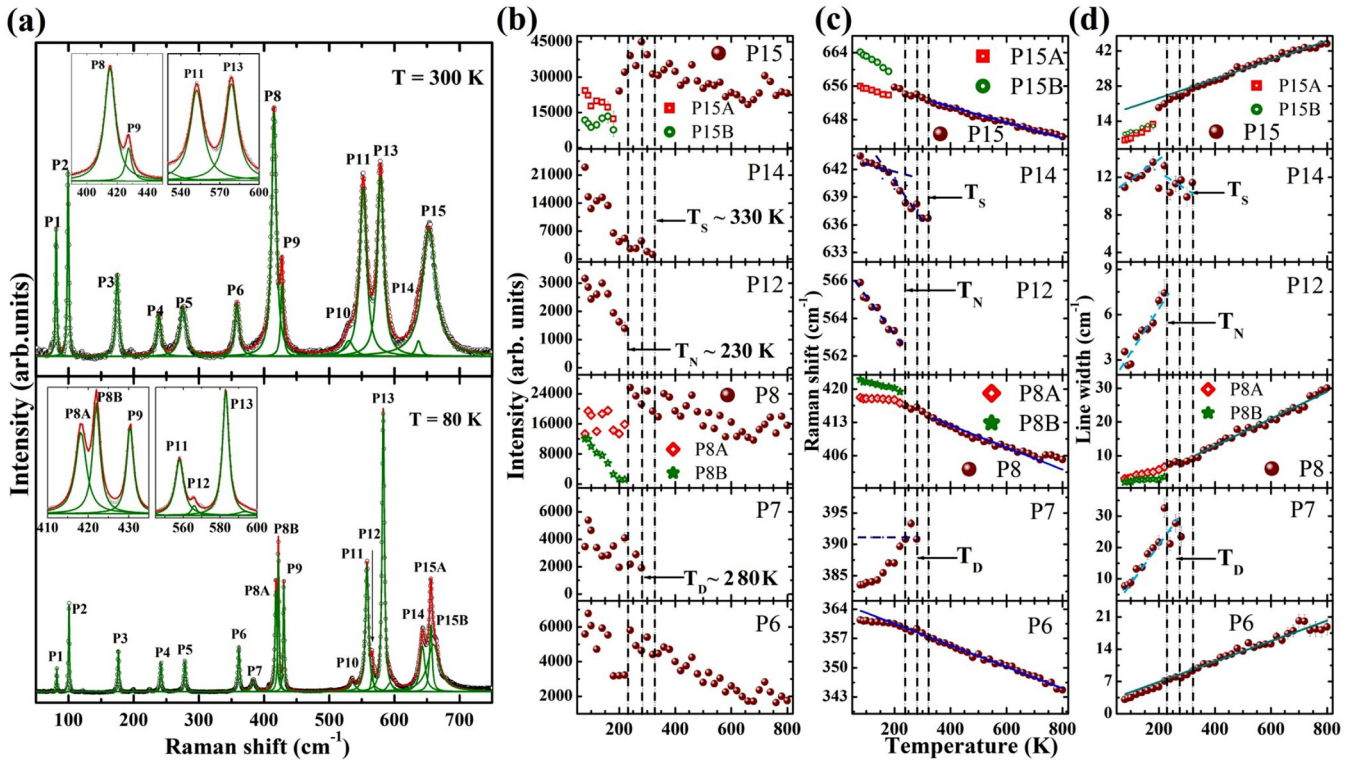
FIG. 3. (a) Raman spectra of 15R-BaMnO$_3$ collected at 80 and 300 K, (b) spectral weight (intensity), (c) frequency, and (d) linewidth of selected phonons are plotted against temperature. Solid lines in (c) and (d) represent the fitting with the anharmonic model [Eqs. (2) and (3) in the text] whereas the dashed lines for modes P12 and P14 below T_N are a guide to the eye. Error bars are smaller than or comparable to the symbol size.

structural phase transition, we attribute the observed anomalies in P6, P7, and P14 phonons to the spin-phonon coupling. The deviations in frequency ($\Delta\omega_{sp-ph}$) in modes P6, P7, and P14 from their anharmonic behaviors (see Fig. 3(c)) with respect to temperature are captured in Fig. 4 which can provide an estimate of the spin-phonon coupling. The strength of spin-phonon coupling is estimated using mean-field and two-spin cluster approximations, as explained below.
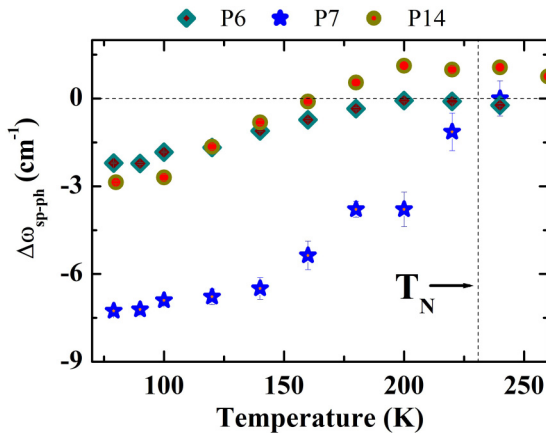

FIG. 4. (a) The deviation of phonon frequency from anharmonic behavior ($\Delta\omega_{sp-ph}$) as a function of temperature (see text). Error bars are within or comparable to the symbol size.

C. Spin-phonon coupling

In magnetic materials, when a phonon is coupled to the spin degrees of freedom, its frequency gets renormalized in proportion to the nearest-neighbor spin-spin correlation function $\langle S_i \cdot S_j \rangle$ (schematically shown in Fig. S10 in the Supplemental Material [27]), which can be written as [41–43]

$$\Delta\omega_{sp-ph} = -\lambda_{sp}\langle S_i \cdot S_j \rangle = -\lambda_{sp}\Phi(T)S^2, \quad (4)$$

where λ_{sp} is the strength of spin-phonon coupling and Φ is the short-range order parameter. Lockwood *et al.* [42] theoretically estimated the $\Phi(T)$ for $S = 2$ (FeF$_2$) and $S = 5/2$ (MnF$_2$) antiferromagnetic systems using mean-field and two-spin cluster approximations. Since the estimates of Φ do not vary much with the value of the spin (S), it was also used reasonably for $S = 1$ (NiF$_2$ and NiO) antiferromagnets [41,43]. Therefore, it is also reasonable to make use of the Φ estimated by Lockwood *et al.* [42] for BaMnO$_3$ in our case where $S = 3/2$ (Mn^{4+}). Thus, the spin-phonon coupling can be estimated using the relation [43]

$$\lambda_{sp} = -\frac{\omega(T_{Low}) - \omega_{anh}(T_{Low})}{[\Phi(T_{Low}) - \Phi(2T_N)]S^2}, \quad (5)$$

where $\omega(T_{Low})$ is the experimental phonon frequency at the lowest temperature recorded ($T_{Low} \sim 80$ K in our case), while $\omega_{anh}(T_{Low})$ is the corresponding anharmonic estimate of the phonon frequency at the same temperature. The obtained values for the spin-phonon coupling (λ_{sp}) for the modes P6, P7, and P14 using Eq. (5) are 1.2, 3.8, and 1.5 cm^{-1},
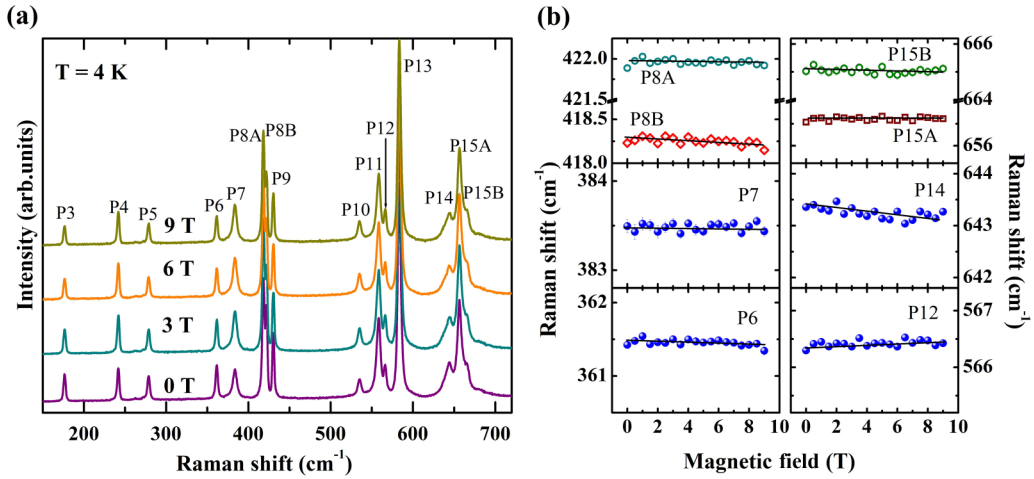
FIG. 5. (a) Raman spectra of 15R-BaMnO$_3$ collected under a few applied magnetic fields at 4 K. (b) The frequency of selected phonons is plotted as a function of magnetic field; solid lines are a guide to the eye showing a decreasing trend with increasing field. Error bars are smaller than the symbol size.

respectively. The coupling strength for the modes is reasonably strong and may be compared with some of the reported values of the strength in compounds such as 9R-BaMnO$_3$ ($\lambda \sim 0.5$–3.4 cm^{-1} [44]), 4H-Sr$_{0.6}$Ba$_{0.4}$MnO$_3$ ($\lambda \sim 2.2$ cm^{-1} [45]), MnF$_2$ ($\lambda \sim 0.4$ cm^{-1} [42]), FeF$_2$ ($\lambda \sim 1.3$ cm^{-1} [42]), La$_2$CoMnO$_6$ ($\lambda \sim 1.7$–2.1 cm^{-1} [46]), Pr$_2$CoMnO$_6$ ($\lambda \sim 0.51$–1.61 cm^{-1} [47,48]), Cr$_2$Ge$_2$Te$_6$ ($\lambda \sim 0.24$–1.2 cm^{-1} [49]), Sr$_2$CoO$_4$ ($\lambda \sim 3.5$ cm^{-1} [50]), NiO ($\lambda \sim -7.9$ and 14.1 cm^{-1} for TO and LO phonons, respectively [43]), ZnCr$_2$O$_4$ ($\lambda \sim 3.2$–6.2 cm^{-1} [51]), NaOsO$_3$ ($\lambda \sim 40$ cm^{-1} [52]), and CuO ($\lambda \sim 50$ cm^{-1} [53]).

D. Emergence of new Raman modes: Effect of magnetostriction

The emergence of new modes in Raman spectra is possible below magnetic transition due to various reasons, such as concurrent magnetic and structural phase transition [54], spin-excitations including one-magnon or two-magnon Raman processes [35,55], or magnetostriction [36,37]. Since phonons and magnetic excitations exhibit contrasting behavior under external magnetic fields, we have investigated the magnetic-field dependence of the Raman spectrum to shed light on the origin of the new modes. 15R-BaMnO$_3$ was cooled down to 4 K and the magnetic field was applied in the range of 0–9 T. Figure 5(a) compares the Raman spectra at 0, 3, 6, and 9 T where no major effect on the spectrum is visible, thus we can rule out the magnetic excitation as the origin for the new modes and assign them as new phonon modes. Figure 5(b) shows the frequency of a few selected phonons as a function of the magnetic field (see also Figs. S11–S14 in the Supplemental Material [27] for phonon parameters). The frequency of all the phonons shows a decreasing trend with increasing magnetic field, thus suggesting a lattice expansion under an external magnetic field, indicating a possible role of magnetostriction.

To ensure any possible role of structural phase transition in the origin of the new phonon modes, we have performed temperature-dependent powder x-ray diffraction measurements (PXRD). Figure 6(a) displays the PXRD pat-

terns collected at a few temperatures in the range of 90–400 K. The number of reflections in the PXRD pattern remains the same in the entire investigated temperature range, and Rietveld analysis of the data confirms the absence of structural phase transition.

In the absence of a structural phase transition, the origin of the new phonon modes below the magnetic transition temperatures could be attributed to the local changes in the symmetry arising from the displacement of Mn-ions at low temperatures. The thermal expansion is a key parameter to ascertain the magnetostriction because it involves the coupling between magnetic and elastic degrees of freedom. We have analyzed the unit-cell parameters (lattice parameters and unit-cell volume) as a function of temperature. Figure 6(b) shows the lattice parameters and unit-cell volume as a function of temperature in the range of 90–450 K (bond lengths are given in Fig. S15 in the Supplemental Material [27]). The 15R-BaMnO$_3$ expands upon heating and shows positive thermal expansion. In general, the temperature-dependent lattice parameters due to thermal expansion can be written as [56]

$$a(T) = a_0 \left[1 + \frac{b e^{\frac{d}{T}}}{T \left(e^{\frac{d}{T}} - 1\right)^2} \right] \quad \text{and}$$

$$c(T) = c_0 \left[1 + \frac{f e^{\frac{g}{T}}}{T \left(e^{\frac{g}{T}} - 1\right)^2} \right], \tag{6}$$

where a_0 and c_0 are the in-plane and out-of-plane lattice constants at 0 K, whereas b, d, f, and g are fitting parameters. Similarly, the unit-cell volume as a function of temperature can be expressed as

$$V(T) = V_0 \left[1 + \frac{A}{\left(e^{\frac{\Theta}{T}} - 1\right)} \right], \tag{7}$$

where V_0 is the cell volume extrapolated to 0 K, Θ is the Debye temperature, and A is a fitting parameter (see Table S4 and Sec. SM7 in the Supplemental Material [27]). Importantly, the temperature dependence of the lattice
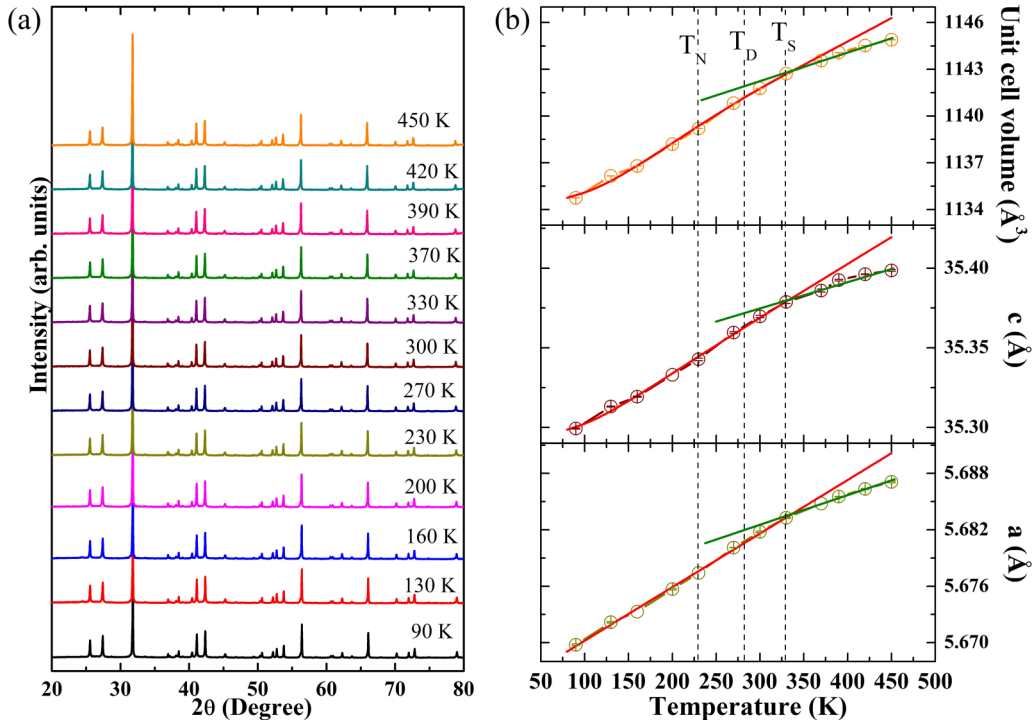
FIG. 6. (a) X-ray diffraction patterns collected at a few temperatures, and (b) unit-cell parameters as a function of temperature; red solid lines represent fittings presenting the expansion [Eqs. (6) and (7) explained in the text], and green solid lines are also fit with Eqs. (6) and (7) showing the deviation from expected behavior. Error bars in (b) are within the symbol size.

parameters and the volume show a deviation at T_S as shown in Fig. 6. As discussed earlier, a short-ranged magnetic ordering occurs below $T_S \sim 330$ K that changes the trend of lattice expansion due to local symmetry changes (without undergoing a structural phase transition), thus corroborating the presence of magnetostriction in 15R-BaMnO$_3$ [57].

It should be noted that the frequency of a phonon $\omega \propto \sqrt{k}$ (k = spring constant), where k decreases with increasing unit-cell volume (bond length). The decrease in phonon frequency with increasing magnetic field, as shown in Fig. 5(b), signifies an expansion of the unit-cell volume under magnetic field, further suggesting the presence of magnetostriction in 15R-BaMnO$_3$. Here, we have quantified the magnetostriction in two ways: (i) using thermal expansion (x-ray diffraction measurements) in the absence of external magnetic field, and (ii) using lattice expansion (Raman spectroscopic measurements) under external magnetic field at a constant temperature.

If the spontaneous distortion in the unit cell (without changing the crystal symmetry) due to magnetic ordering is large enough, it can be detected by the x-ray diffraction technique, which also provides several advantages over conventional strain-gauge and capacitive techniques [57–59]. The spontaneous volume magnetostriction [$\lambda_{\mathrm{ms}}^{V}(T)$] at a given temperature "T" (below T_N) can be defined as [61]

$$\lambda_{\mathrm{ms}}^{V}(T) = \frac{V_{\mathrm{AFM}}(T) - V_{\mathrm{PM}}(T)}{V_{\mathrm{PM}}(T)}, \qquad (8)$$

where $V_{\mathrm{AFM}}(T)$ is the actual unit-cell volume at the temperature T in the antiferromagnetic phase, whereas $V_{\mathrm{PM}}(T)$

is the hypothetical volume of the unit cell if it were in the paramagnetic (nonmagnetic) phase at the same temperature. The value of $\lambda_{\mathrm{ms}}^{V}$ at 90 K (lowest measured temperature) is $\sim 32(\pm 7) \times 10^{-4}$, which is comparable to the reported value of magnetostriction in the spinel compounds Zn$_{1-x}$Cu$_x$Cr$_2$Se$_4$ [$(4.6$–$24.9) \times 10^{-4}$ at 100 K for varying x] measured by the XRD technique [61] (temperature-dependent values of $\lambda_{\mathrm{ms}}^{V}$ for 15RBaMnO$_3$ are given in Fig. S16 in the Supplemental Material [27]).

On the other hand, magnetostriction can also be defined as the change in the dimensions of a magnetic material under an external magnetic field. It is often characterized by $\frac{\Delta l}{l}$, where l is the original physical length of the material and dl is the change in the dimension of the material under the applied magnetic field (H) [60]. It can be expressed as $\lambda_{\mathrm{ms}}^{l} = \frac{\Delta l}{l} \approx \frac{l(H) - l(0)}{l(0)}$ for the linear magnetostriction, and similarly the volume magnetostriction is $\lambda_{\mathrm{ms}}^{V} = \frac{\Delta V}{V} \approx \frac{V(H) - V(0)}{V(0)}$, where for our case we have considered the unit-cell dimensions instead of the physical dimensions. The change in unit-cell volume can be related to the corresponding change in phonon frequency through the Grüneisen parameter as $\frac{\Delta \omega}{\omega} = \gamma \frac{\Delta V}{V}$. In solids, the typical value of the mode Grüneisen parameter (γ) is ~ 1 (see the Supplemental Material [27] for details). Under the assumption of $\gamma \sim 1$, the volume magnetostriction of 15R-BaMnO$_3$ at 4 K is estimated to be in the range of $(0.01$–$5.6) \times 10^{-4}$ (Fig. S21 in the Supplemental Material [27]), which is comparable to the range of reported magnetostriction values (10^{-3}–10^{-6}) in various systems [62–68] and also comparable to the value obtained through the x-ray diffraction technique discussed above (see Figs. S17–21

and Table S5 in Sec. SM8 of the Supplemental Material [27] for details on estimation of γ and magnetostriction in 15R-BaMnO$_3$).

IV. CONCLUSIONS

In summary, we have synthesized polycrystalline hexagonal BaMnO$_3$ in 15R phase using the solid-state reaction route. A new phonon of frequency ~ 390 cm^{-1} (P7), associated with Mn vibrations, appears below ~ 280 K (due to local distortions arising from the displacement of Mn-ions) and exhibits anomalous behavior due to strong spin-phonon coupling ($\lambda_{sp-ph} \sim 3.8$ cm^{-1}). Additionally, several new modes appear below the magnetic transition temperatures (330 and 230 K) due to the local changes in symmetry arising from the displacement of Mn ions. Further, we have observed evidence of magnetostriction in 15R-BaMnO$_3$ through a change in the lattice expansion rate across the magnetic ordering temperature in XRD measurements and signatures of lattice expansion under applied magnetic field in Raman scattering. We have

shown that the lattice vibrations are strongly correlated with the electric and magnetic properties in 15R-BaMnO$_3$. We believe that the spin-phonon coupling and lattice strain (magnetostriction) can be the new parameters to tune the magnetoelectric properties of the system, thus there is a potential for near room-temperature technological applications, and this will motivate further experimental and theoretical studies.

[1] J. Orenstein and A. J. Millis, Advances in the physics of high-temperature superconductivity, Science **288**, 468 (2000).

[2] W. Eerenstein, N. D. Mathur, and J. F. Scott, Multiferroic and magnetoelectric materials, Nature (London) **442**, 759 (2006).

[3] T. Ideue, T. Kurumaji, S. Ishiwata, and Y. Tokura, Giant thermal hall effect in multiferroics, Nat. Mater. **16**, 797 (2017).

[4] D. I. Khomskii and G. A. Sawatzky, Interplay between spin, charge and orbital degrees of freedom in magnetic oxides, Solid State Commun. **102**, 87 (1997).

[5] S. F. Maehrlein, I. Radu, P. Maldonado, A. Paarmann, M. Gensch, A. M. Kalashnikova, R. V. Pisarev, M. Wolf, P. M. Oppeneer, J. Barker, and T. Kampfrath, Dissecting spin-phonon equilibration in ferrimagnetic insulators by ultrafast lattice excitation, Sci. Adv. **4**, eaar5164 (2018).

[6] X. Moya and N. D. Mathur, Thermal hall effect: turn your phonon, Nat. Mater. **16**, 784 (2017).

[7] M. Bibes and A. Barthélémy, Multiferroics: towards a magnetoelectric memory, Nat. Mater. **7**, 425 (2008).

[8] T. Jungwirth, X. Marti, P. Waldley, and J. Wunderlich, Antiferromagnetic spintronics, Nat. Nanotechnol. **11**, 231 (2016).

[9] T. Jungwirth, J. Sinova, A. Manchon, X. Marti, J. Wunderlich, and C. Felser, The multiple directions of antiferromagnetic spintronics, Nat. Phys. **14**, 200 (2018).

[10] P. Němec, M. Fiebig, T. Kampfrath, and A. V. Kimel, Antiferromagnetic opto-spintronics, Nat. Phys. **14**, 229 (2018).

[11] J. H. Lee, L. Fang, E. Vlahos, X. Ke, Y. W. Jung, L. F. Kourkoutis, J.-W. Kim, P. J. Ryan, T. Heeg, M. Roeckerath, V. Goian, M. Bernhagen, R. Uecker, P. C. Hammel, K. M. Rabe, S. Kamba, J. Schubert, J. W. Freeland, D. A. Muller, C. J. Fennie, P. Schiffer, V. Gopalan, E. Johnston-Halperin, and D. G. Schlom, A strong ferroelectric ferromagnet created by means of spin-lattice coupling, Nature (London) **466**, 954 (2010).

[12] M. Mochizuki, N. Furukawa, and N. Nagaosa, Theory of spin-phonon coupling in multiferroic manganese perovskites RMnO$_3$, Phys. Rev. B **84**, 144409 (2011).

[13] C. Calero, E. M. Chudnovsky, and D. A. Garanin, Field Dependence of the Electron Spin Relaxation in Quantum Dots, Phys. Rev. Lett. **95**, 166603 (2005).

[14] D. Khomskii, Classifying multiferroics: Mechanisms and effects, Physics **2**, 20 (2009).

[15] O. B. Korneta, T. F. Qi, M. Ge, S. Parkin, L. E. De Long, P. Schlottmann, and G. Cao, Correlated giant dielectric peaks and antiferromagnetic transitions near room temperature in pure and alkali-doped BaMnO$_{3-\delta}$, J. Phys.: Condens. Matter **23**, 435901 (2011).

[16] T. Nakamura, Soft phonon in BaTiO$_3$, J. Ferroelectr. **137**, 65 (1992).

[17] Y. Luspint, J. L. Servoin, and F. Gervais, Soft mode spectroscopy in barium titanate, J. Phys. C **13**, 3761 (1980).

[18] B. Poojitha, K. Rubi, S. Sarkar, R. Mahendiran, T. Venkatesan, and S. Saha, Effect of phonon anharmonicity on ferroelectricity in Eu$_x$Ba$_{1-x}$TiO$_3$, Phys. Rev. Mater. **3**, 024412 (2019).

[19] T. A. Tyson, T. Wu, K. H. Ahn, S.-B. Kim, and S.-W. Cheong, Local spin-coupled distortions in multiferroic hexagonal HoMnO$_3$, Phys. Rev. B **81**, 054101 (2010).

[20] T. E. Saunders and J. T. Chalker, Structural phase transitions in geometrically frustrated antiferromagnets, Phys. Rev. B **77**, 214438 (2008).

[21] I. P. Handayani, A. A. Nugroho, S. Riyadi, G. R. Blake, N. Mufti, T. T. M. Palstra, and P. H. M. van Loosdrecht, Correlation between lattice vibrations with charge, orbital, and spin ordering in the layered manganite Pr$_{0.5}$Ca$_{1.5}$MnO$_4$, Phys. Rev. B **92**, 205101 (2015).

[22] A. Nonato, B. S. Araujo, A. P. Ayala, A. P. Maciel, S. Yanez-Vilar, M. Sanchez-Andujar, M. A. Senaris-Rodriguez, and C. W. A. Paschoal1, Spin-phonon and magnetostriction phenomena in CaMn$_7$O$_{12}$ helimagnet probed by Raman spectroscopy, Appl. Phys. Lett. **105**, 222902 (2014).

[23] V. G. Sathe, S. Tyagi, and G. Sharma, Electron-phonon coupling in perovskites studied by Raman Scattering, J. Phys. Conf. Ser. **755**, 012008 (2016).

[24] K. Momma and F. Izumi, VESTA 3 for three-dimensional visualization of crystal, volumetric and morphology data, J. Appl. Cryst. **44**, 1272 (2011).

[25] J. J. Adkin and M. A. Hayward, $BaMnO_{3-x}$ revisited: a structural and magnetic study, Chem. Mater. **19**, 755 (2007).

[26] D. P. Kozlenko, N. T. Dang, T. L. Phan, S. E. Kichanov, L. H. Khiem, S. G. Jabarov, T. A. Tran, T. V. Manh, A. T. Le, T. K. Nguyen, and B. N. Savenko, The structural, magnetic and vibrational properties of Ti-doped $BaMnO_3$, J. Alloys Compd. **695**, 2539 (2017).

[27] See Supplemental Material at http://link.aps.org/supplemental/10.1103/PhysRevB.102.134436 for additional data and information about the magnetic and heat capacity measurements, assignment of modes, polarization-, temperature-, and magnetic-field-dependent Raman spectra, and powder XRD data.

[28] R. J. D. Tilley, *Perovskites, Structure-Property Relationships*, 1st ed. (Wiley, UK, 2016).

[29] P. D. Battle, T. C. Gibb, and C. W. Jones, The structural and magnetic properties of $SrMnO_3$: A reinvestigation, J. Solid State Chem. **74**, 60 (1988).

[30] L. Ghivelder, I. A. Castillo, N. McN. Alford, G. J. Tomka, P. C. Riedi, J. M. Manus-Driscoll, A. K. M. A. Hossain, and L. F. Cohen, Specific heat of $La_{1-x}Ca_xMnO_{3-d}$, J. Magn. Magn. Mater. **189**, 274 (1998).

[31] B. F. Woodfield, M. L. Wilson, and J. M. Byers, Low-Temperature Specific Heat of $La_{1-x}Sr_xMnO_{3+d}$, Phys. Rev. Lett. **78**, 3201 (1997).

[32] E. Kroumova, M. I. Aroyo, J. M. Perez-Mato, A. Kirov, C. Capillas, S. Ivantchev, and H. Wondratschek, Bilbao crystallographic server: useful databases and tools for phase-transition studies, Phase Trans. **76**, 155 (2003).

[33] C. Xiang-Bai, H. N. T. Minh, Y. In-Sang, L. E. E. Daesu, and N. O. H. Tae-Won, A raman study of the origin of oxygen defects in hexagonal manganite thin films, Chin. Phys. Lett. **29**, 126103 (2012).

[34] R. A. Evarestov and A. V. Bandura, First-principles calculations on the four phases of $BaTiO_3$, J. Comput. Chem. **33**, 1123 (2012).

[35] P. A. Fleury, Paramagnetic spin waves and correlation functions in NiF_2, Phys. Rev. **180**, 591 (1969).

[36] H. C. Hsu, F. C. Chou, K. Koyama, K. Watanabe, and H. L. Liu, Spin-phonon coupling in antiferromagnetic $Bi_2Sr_2CoO_{6+\delta}$: an infrared reflectance study, Phys. Rev. B **79**, 155109 (2009).

[37] C. Toulouse, C. Martin, M.-A. Measson, Y. Gallais, A. Sacuto, and M. Cazayous, Magnetic transitions in $CaMn_7O_{12}$: Raman observation of spin-phonon couplings, Phys. Rev. B **99**, 024303 (2019).

[38] S. Xie, E. Iglesia, and A. T. Bell, Effects of temperature on the Raman spectra and dispersed oxides, J. Phys. Chem. B **105**, 5144 (2001).

[39] M. Balkanski, R. F. Wallis, and E. Haro, Anharmonic effects in light scattering due to optical phonons in silicon, Phys. Rev. B **28**, 1928 (1983).

[40] P. G. Klemens, Anharmonic decay of optical phonons, Phys. Rev. **148**, 845 (1966).

[41] D. J. Lockwood, Spin-phonon interaction and mode softening in NiF_2, Low Temp. Phys. **28**, 505 (2002).

[42] D. J. Lockwood and M. G. Cottam, The spin-phonon interaction in FeF_2 and MnF_2 studied by Raman spectroscopy, J. Appl. Phys. **64**, 5876 (1988).

[43] E. Atyan, B. Debnath, F. Kargar, Y. Barlas, M. M. Lacerda, J. X. Li, R. K. Lake, J. Shi, and A. A. Balandin, Spin-phonon coupling in antiferromagnetic nickel oxide, Appl. Phys. Lett. **111**, 252402 (2017).

[44] B. Poojitha, A. Rathore, and S. Saha, Spin-phonon coupling in Sr and Ti incorporated 9R-$BaMnO_3$, J. Magn. Magn. Mater. **483**, 212 (2019).

[45] R. Rawat, D. M. Phase, and R. J. Choudhary, Spin-phonon coupling in hexagonal $Sr_{0.6}Ba_{0.4}MnO_3$, J. Magn. Magn. Mater. **441**, 398 (2017).

[46] C. Meyer, V. Roddatis, P. Ksoll, B. Damaschke, and V. Moshnyaga, Structure, magnetism, and spin-phonon coupling in heteroepitaxial $La_2CoMnO_6/Al_2O_3(0001)$ films, Phys. Rev. B **98**, 134433 (2018).

[47] D. Kumar, S. Kumar, and V. G. Sathe, Spin-phonon coupling in ordered double perovskites A_2CoMnO_6 (A = La, Pr, Nd) probed by micro-Raman spectroscopy, Solid State Commun. **194**, 59 (2014).

[48] C. Xie, L. Shi, J. Zhao, S. Zhou, Y. Li, and X. Yuan, Spin-phonon coupling in R_2CoMnO_6 (R = Pr, Nd, Sm) thin films under biaxial compressive strain, J. Appl. Phys. **120**, 155302 (2016).

[49] Y. Tian, M. J. Gray, H. Ji, R. J. Cava, and K. S. Burch, Magneto-elastic coupling in a potential ferromagnetic 2D atomic crystal, 2D Mater. **3**, 025035 (2016).

[50] P. K. Pandey, R. J. Choudhary, D. K. Mishra, V. G. Sathe, and D. M. Phase, Signature of spin-phonon coupling in Sr_2CoO_4 thin film: a raman spectroscopic study, Appl. Phys. Lett. **102**, 142401 (2013).

[51] A. B. Sushkov, O. Tchernyshyov, W. Ratcliff II, S. W. Cheong, and H. D. Drew, Probing Spin Correlations with Phonons in the Strongly Frustrated Magnet $ZnCr_2O_4$, Phys. Rev. Lett. **94**, 137202 (2005).

[52] S. Calder *et al.*, Enhanced spin-phonon-electronic coupling in a 5d oxide, Nat. Commun. **6**, 8916 (2015).

[53] X. K. Chen, J. C. Irwin, and J. P. Franck, Evidence for a strong spin-phonon interaction in cupric oxide, Phys. Rev. B **52**, R13130(R) (1995).

[54] T. N. Stanislavchuk, A. P. Litvinchuk, R. Hu, Y. H. Jeon, S. D. Ji, S. W. Cheong, and A. A. Sirenko, Optical properties, lattice dynamics, and structural phase transition in hexagonal 2H-$BaMnO_3$ single crystals, Phys. Rev. B **92**, 134308 (2015).

[55] P. A. Fleury, S. P. S. Porto, L. E. Cheesman, and H. J. Guggenheim, Light Scattering by Spin Waves in FeF_2, Phys. Rev. Lett. **17**, 84 (1966).

[56] C. Kittel, *Introduction to Solid State Physics*, 7th ed. (Wiley, New York, 2003).

[57] F. J. Darnell, Temperature dependence of lattice parameters for Gd, Dy, and Ho, Phys. Rev. **130**, 1825 (1963).

[58] F. J. Darnell, Magnetostriction in dysprosium and terbium, Phys. Rev. **132**, 128 (1963).

[59] J. Samuel Smart and S. Greenwald, Crystal structure transitions in antiferromagnetic compounds at the curie temperature, Phys. Rev. **82**, 113 (1951).

[60] B. K. Tanner, Diffraction techniques in the study of magnetic domains and magnetostriction, Sci. Prog., Oxf. **67**, 411 (1981).

[61] J. Kusz, S. Juszczyk, and J. Warczewski, An x-ray diffraction study of magnetostriction in $Zn_{1-x}Cu_xCr_2Se_4$ ($0.2 < x < 1.0$), J. Appl. Cryst. **21**, 898 (1988).

[62] P. N. Anantharamaiah and P. A. Joy, Enhancing the strain sensitivity of $CoFe_2O_4$ at low magnetic fields without affecting the magnetostriction coefficient by substitution of small amounts of Mg for Fe, Phys. Chem. Chem. Phys., **18**, 10516 (2016).

[63] M. Doerr, M. Rotter, and A. Lindbaum, Magnetostriction in rare-earth based antiferromagnets, Adv. Phys. **54**, 1 (2005).

[64] S. S. Fonton and A. V. Zalesskiǐ, Magnetostriction of a single crystal of hexagonal ferrite $BaFe_{18}O_{27}$, J. Exptl. Theoret. Phys. (U.S.S.R.) **47**, 1693 (1964) [Sov. Phys. JETP **20**, 1138 (1965)].

[65] E. Klokholm and J. Aboaf, The saturation magnetostriction of thin polycrystalline films of iron, cobalt, and nickel, J. Appl. Phys. **53**, 2661 (1982).

[66] A. Majumder, K. Ugendar, K. B. Anoop Baby, V. Chunchu, R. A. Mondal, and G. Markandeyulu, Anisotropy, magnetostriction and converse magnetoelectric effect in Dy substituted Ni ferrite, Phys. Proc. **75**, 238 (2015).

[67] A. B. Smith and R. V. Jones, Magnetostriction in nickel ferrite and cobalt-nickel ferrite, J. Appl. Phys. **37**, 1001 (1966).

[68] J. Smit and H. P. J. Wijn, Ferrites, *Philips Technical Library* (Eindhoven, The Netherlands, 1959).